Design, Manufacture, and Characterization of a Carbon Fiber-Reinforced Silicon Carbide Nozzle Extension

Fabian Breede,* Severin Hofmann, Neraj Jain and Raouf Jemmali

Institute of Structures and Design, German Aerospace Center (DLR), Pfaffenwaldring 38–40, Stuttgart 70569, Germany

Nozzle extensions made of ceramic matrix composites (CMCs) have shown the potential to replace heavy superalloy nozzles and improve the performance of future upper-stage and orbital rocket engines. Gas permeability has been reported to be a critical issue during the manufacture for CMC nozzles. This work shows the manufacture of a dense radiation-cooled C/C-SiC nozzle demonstrator. A multi-angle fiber architecture was applied using filament winding technique to reduce the incidence of delaminations during the manufacturing process under high temperatures. Additional efforts were made to improve the final gas tightness and reduce the amount of residual silicon by means of an adapted liquid silicon infiltration process. The manufacture, the material, and structural characterization as well as a finite element analysis of a performed internal pressure test are presented.

Introduction

Carbon fiber-reinforced silicon carbide matrix composites are one of the most promising material alternatives to the heavy superalloys for applications in rocket propulsion, such as rocket nozzle extensions. Due to their excellent thermal and mechanical properties at high temperatures and due to their low material density, they will increase the payload capacity and improve the performance of future upper-stage and orbital rocket engines.[1–5]

A variety of different ceramic matrix composite (CMC) processing routes have been studied intensively during the last 10 years, including chemical vapor infiltration (CVI),[6–9] liquid polymer infiltration and pyrolysis (PIP),[10,11] and reactive melt infiltration,[12–16] and combinations of these. Processing costs and durations are significantly high using CVI or PIP fabrication routes. These CMC materials require a complex fiber coating (fiber–matrix interface) to obtain a damage tolerant fracture behavior, and they usually also exhibit high open porosity because of their specific processing. On the other hand, CMC materials made by LSI feature short processing times (3–4 weeks) and cheap raw materials (C-fiber, C-precursor and silicon) which are commercially available. Within adapted C/C-SiC materials made by LSI, no fiber coating is needed because carbon filaments are embedded in a dense carbon matrix which is surrounded by silicon carbide and residual silicon.[17–19] This results in low open porosity values which are favorable as dense CMC materials are usually required for most nozzle skirt applications.

The Institute of Structures and Design of the German Aerospace Center (DLR) has been working on advanced C/C-SiC composites for future thermal protection and space propulsion systems.[20–22] Within the last years, a processing route has been developed to manufacture novel high-strength C/C-SiC rocket nozzle extensions using filament winding technique in combination with an adapted liquid silicon infiltration process which leads to dense axisymmetric CMC structures. The main advantage over comparable standard tape-wound structures is that using a wet filament winding technique, the nozzle fiber preform and carbon precursor impregnation with subsequent curing is performed in one efficient process, whereas the dry tape-wound approach needs an additional infiltration process that usually requires complex molds. Also, most tape-wound structures use thermoplastic resins, whereas for C/C-SiC materials in this study, phenolic precursors are required to produce the desired microstructure to provide good mechanical performance. Another recent example of carbon fiber-reinforced silicon carbide composite nozzle material was presented by Kumar *et al.*[23] In contrast to the material presented by Kumar *et al.*, which showed a rather high material density of about 2.3 g/cm^3 and a lower overall mechanical performance due to carbon fiber degradation during siliconization, the presented C/C-SiC material in

*fabian.breede@dlr.de

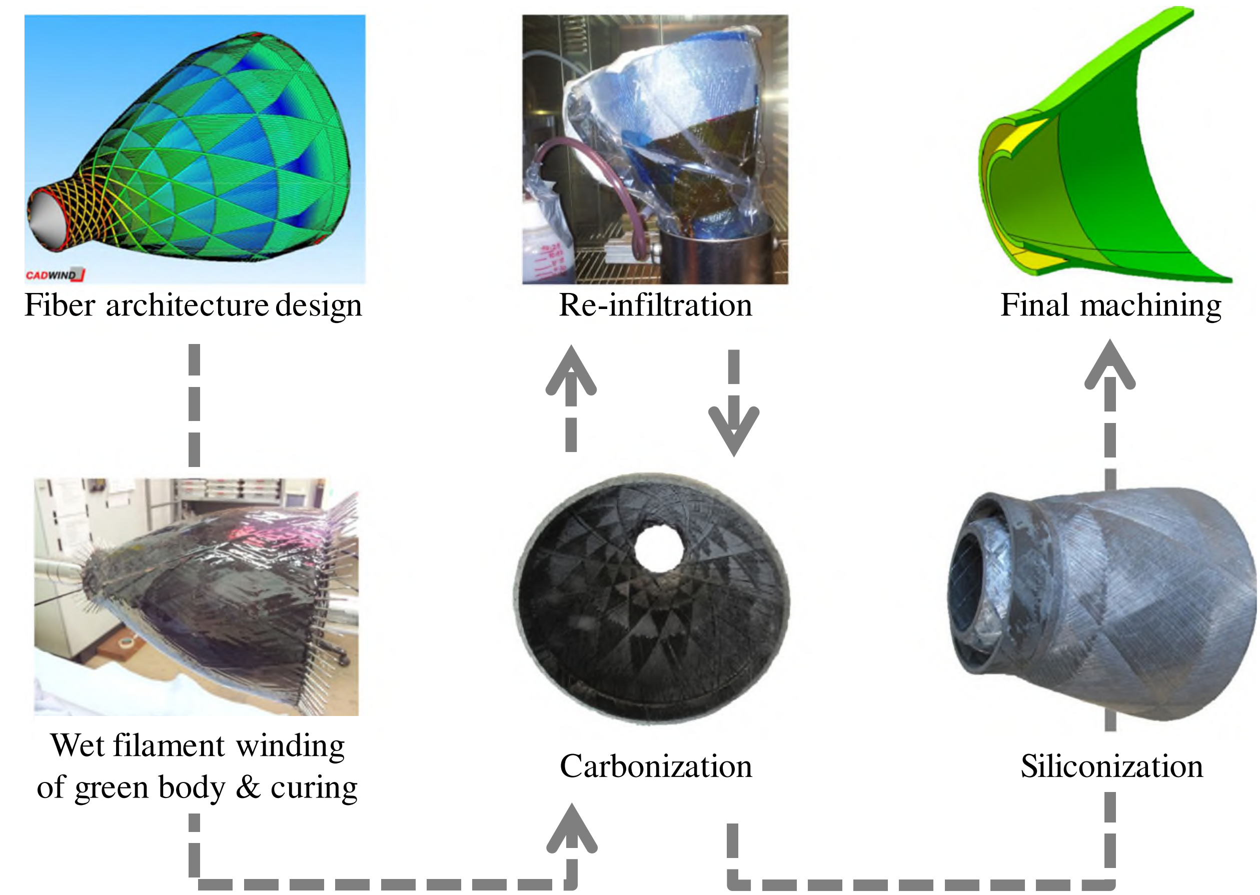

Fig. 1. Manufacturing process scheme of DLR's C/C-SiC nozzle extensions.

this study provides an improved microstructure suitable for highly mechanically loaded CMC nozzle structures.

This work presents the design and manufacture as well as the main material and structural characterization results of a partially double-walled radiation-cooled C/C-SiC nozzle extension. The main goal of this work was to show the advantages and the viability of a C/C-SiC nozzle structure made by LSI, which was demonstrated with preliminary hot-firing tests within DLR's experimental full-ceramic thrust chamber test campaign.

Manufacture

At DLR, the C/C-SiC nozzle structures are currently manufactured using the filament winding technique, and an adapted liquid silicon infiltration process (Fig. 1). The main steps in the manufacturing process are as follows:

- Design of the fiber architecture,
- Wet filament winding of the nozzle green body and curing,
- Carbonization (pyrolysis),
- Re-infiltration with a polymer and carbonization,
- Liquid silicon infiltration (siliconization),
- Final machining,
- Application of an environmental barrier coating (optional).

The nozzle follows a truncated ideal contour with a total length of about 200 mm and an exit diameter of about 220 mm, which corresponds to an expansion ratio[1] of about 120. The nozzle start area ratio is 12.

Cadwind V9 Expert filament winding software (Materials, Brussels, Belgium) was used to design and develop the desired fiber architecture because it has a complex divergent wall contour that consists of increasing diameters in axial direction. The fiber preforms were

[1]Expansion ratio ε, also called nozzle area ratio, is the cross-sectional area of the nozzle exit divided by the cross-sectional area of the nozzle throat, $\epsilon, = A_x/A_{\mathrm{throat}}$

fabricated using a three-axis filament winding machine by *Waltritsch & Wachter*.

The contour geometry of the winding mandrel is provided to Cadwind, and it generates a model with several fiber layers with varying fiber orientations. Filament winding theory places limitations on the number of different fiber orientations that can be used.[24] Figure 2 depicts the geometry of the mandrel contour used to manufacture the double-walled nozzle.

Generally, the design of the fiber architecture is a compromise between structural design requirements (mechanical and thermal loads, etc.), the processing-related effects such as shrinkage, and the limitations of the winding technique.

To mitigate the risk of shrinkage-induced delaminations, the fiber architecture was adapted to process the shrinkage effects of the fiber preform during the carbonization processing step. Note, two consecutive layers with the same fiber orientation theoretically result in a gap (delamination; Fig. 3). The circumferential shrinkage of each fiber layer depends on the winding angle α, which is here defined as the fiber orientation with respect to the axis of rotation (Fig. 4a). The circumferential shrinkage $\Delta U/U$ can be calculated from the local shrinkage values ($\Delta x/x$, $\Delta y/y$ and $\Delta z/z$), which can be estimated from experimental shrinkage values of wound C/C-SiC plates with an small fiber orientation (e.g., $\pm 15°$), resulting in an approximation to an unidirectional composite. The circumferential shrinkage increases with decreasing winding angles (Fig. 4b); therefore, each consecutive fiber layer should have a smaller winding angle than its predecessor. This multiangle fiber architecture approach reduces the incidence of delaminations among the fiber layers as outer fiber layers tend to shrink onto inner layers, applying compression. However, winding boundary conditions associated with the mandrel's complex geometry or load-specific design requirements may limit the extent to which this favorable fiber architecture design can be implemented.

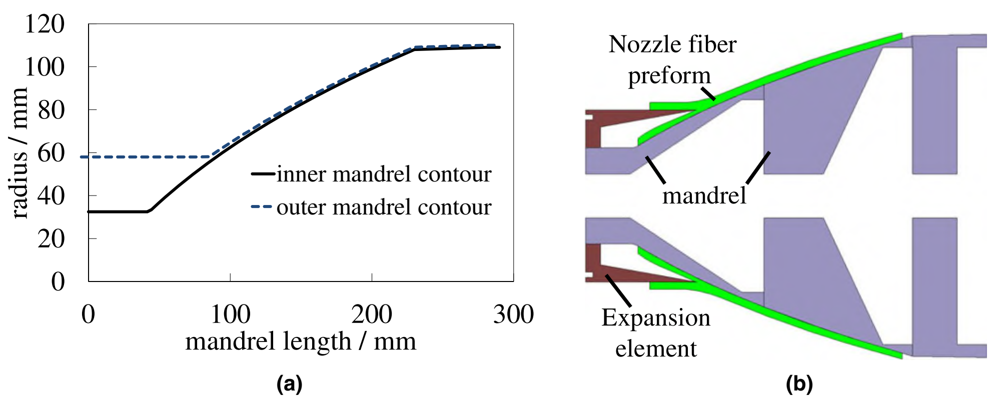

Fig. 2. Mandrel contours (a) and design sketch of mandrel assembly (b).

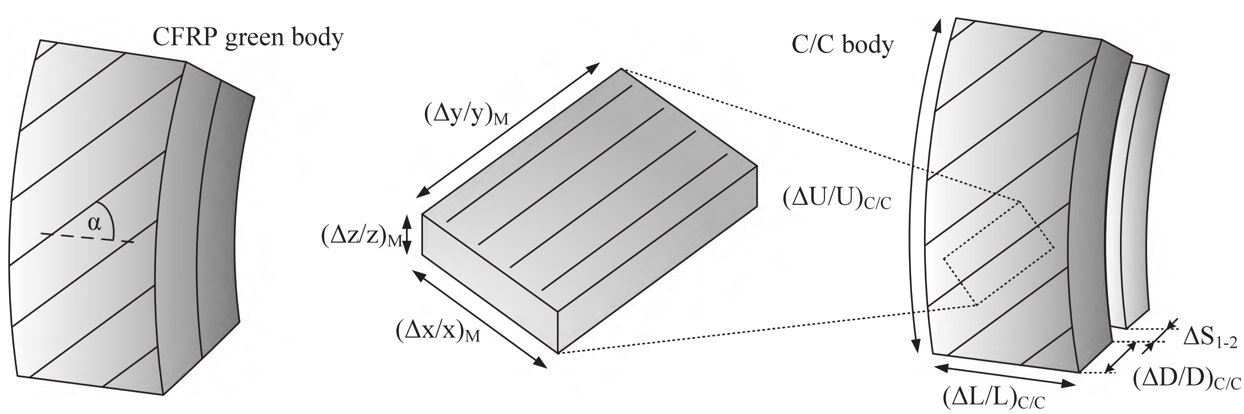

Fig. 3. Illustration of the general theoretical shrinkage phenomena during carbonization of filament wound structures.

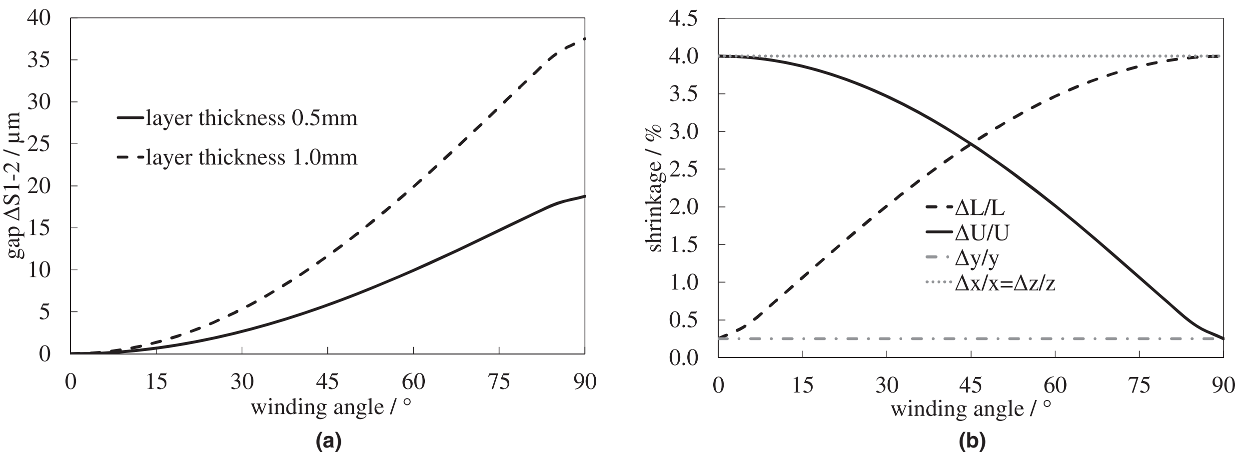

Fig. 4. Theoretical gap size during carbonization of layers with identical winding angles (a) and simplified evolution of shrinkage values for different fiber orientations (b).

The nozzle preform was made of nine nongeodesic cross-winding fiber layers (Fig. 5). Layers 1–3 represent the inner nozzle shell that was wound on the inner mandrel contour; and layers 4–9 provide the outer shell for the interface and also contribute to the wall thickness toward the nozzle exit. Table I presents the specifications of the multi-angle fiber architecture that was used in the nozzle preform; the desired multi-angle fiber architecture with decreasing winding angles for each consecutive layer was achieved. The choice of winding path and the winding angle, between the nozzle exit and the interface position, were provided by Cadwind, which performed the non-geodesic winding calculations.

The nozzle preform was manufactured by wet filament winding, using a Toray T800 12K continuous carbon fiber tow (Toray Industries, SOFICAR, Paris, France) and a phenolic resin. The resulting high-strength C/C-SiC material, using the combination of T800 fibers and a phenolic resin, provides a better microstructure and consequently superior mechanical properties than those made using the less expensive T300 fibers, as presented in other studies.[14,25]

Table I. Multi-Angle Fiber Architecture With Exemplary Winding Angles α for Each Fiber Layer at the Interface and Nozzle Exit Position

Layer no.	1	2	3	4	5	6	7	8	9
$\alpha_{interface}/°$	60	55	50	60	55	50	45	40	45
$\alpha_{nozzleexit}/°$	28	28	28	45	42	40	38	35	35

The fiber tow was impregnated with a high carbon yield phenolic precursor immediately before being wound on the mandrel. After winding layers 1–3, an expansion element was used to provide the outer mandrel contour for continuation of winding layers 4–9

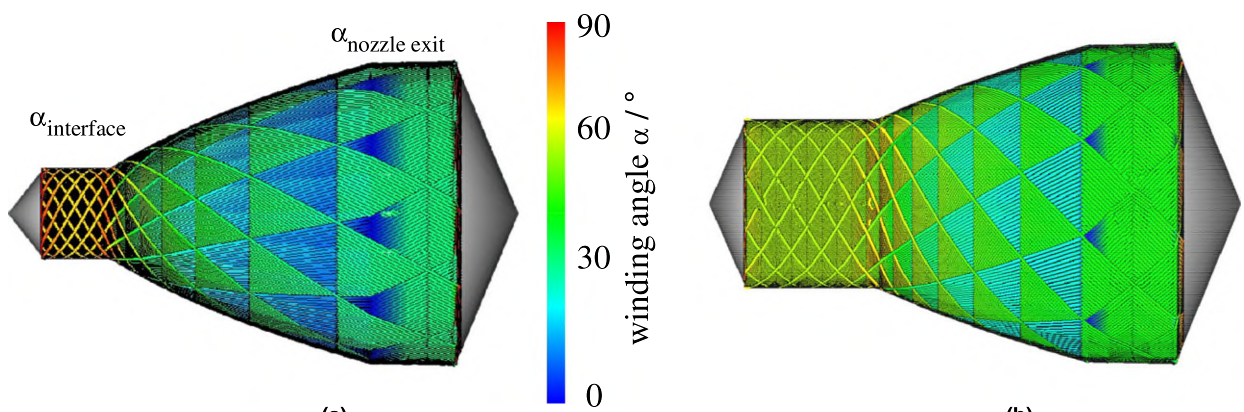

Fig. 5. Exemplary cross-winding pattern for layer no. 1 (a) and layer no. 4 (b).

(Figs. 2 and 5). After the winding process, the wet nozzle fiber preform was cured at 200°C for 3 h at 8 bar in an autoclave, producing a carbon fiber reinforced plastic (CFRP) green body. Note that no outer molds were used for additional consolidation to provide a simple and efficient curing process. Delaminations between layers and voids during curing are mitigated by a well-defined wound fiber architecture, and effective impregnation of the fiber tow. The mandrel was removed after cooling to room temperature.

Then, the CFRP green body was pyrolyzed into a C/C body. Carbonization was performed at a maximum temperature of 1450°C in inert gas conditions during a period of 3 days. During carbonization, the polymer matrix was converted to amorphous carbon resulting in a volumetric contraction and mass reduction of the polymer, creating a porous C/C composite. The volumetric carbon yield of this phenolic precursor is about 46% at 1450°C. Generally, this process forms small C/C segments inside the material where carbon fibers are embedded in a dense carbon matrix and are interconnected by a pore and crack system, which constitutes the open porosity. To avoid any nozzle contour deformations and ovalization due to the shrinkage effects during pyrolysis, the inner nozzle contour was supported with graphite cores with the same shape and size as the mandrel.

The C/C-skeleton undergoes re-infiltration after the first pyrolysis to reduce the open porosity and thereby reduce the amount of residual silicon that will remain after the liquid silicon infiltration process, consequently improving the CMC's microstructure and mechanical properties. The re-infiltration process is based on a vacuum-assisted resin infiltration method using a vacuum bag to form a net-shape mold. The C/C composite was then infiltrated with an other phenolic precursor based on furfuryl alcohol and cured at 150°C for 3 h at 8 bar. The second pyrolysis was performed under the same conditions as the first. The volumetric carbon yield of the second phenolic precursor is about 30% at 1450°C.

During the last processing step, the C/C nozzle structure was infiltrated with liquid silicon by means of capillary forces at a maximum temperature of 1450°C within 3 h during a period of 2 days. Porous reaction-sintered silicon carbide plates were used as part of a wick infiltration method to provide silicon granulate at the top and at the bottom of the nozzle to ensure a homogeneous silicon infiltration. When the silicon melts, it infiltrates the nozzle structure and immediately reacts with the accessible carbon surfaces to form silicon carbide.

In general, the final microstructure is characterized by carbon fibers embedded in carbon matrix segments, surrounded by a layer of silicon carbide; for this reason, the material is named C/C-SiC.[17] Depending on the morphology and open porosity, some unreacted silicon remains in the material. Mechanical properties and the damage accumulation behavior of comparable C/C-SiC material were recently published in Breede *et al.*[26]

The C/C-SiC nozzle extension was truncated to the desired nozzle length and interface position. To improve the oxidation resistance of the C/C-SiC material during hot-firing tests, a environmental barrier coating (100–200 μm) was deposited onto final nozzle structure at MT Aerospace, Augsburg, Germany. The final nozzle structure is illustrated in Fig. 6 and Table II summarizes same general specifications.

Characterization Methods

This section provides a short overview of the methods used to perform the material and structural characterization of the manufactured nozzle extension.

The material density and the open porosity were measured after each manufacturing step using the Archi-

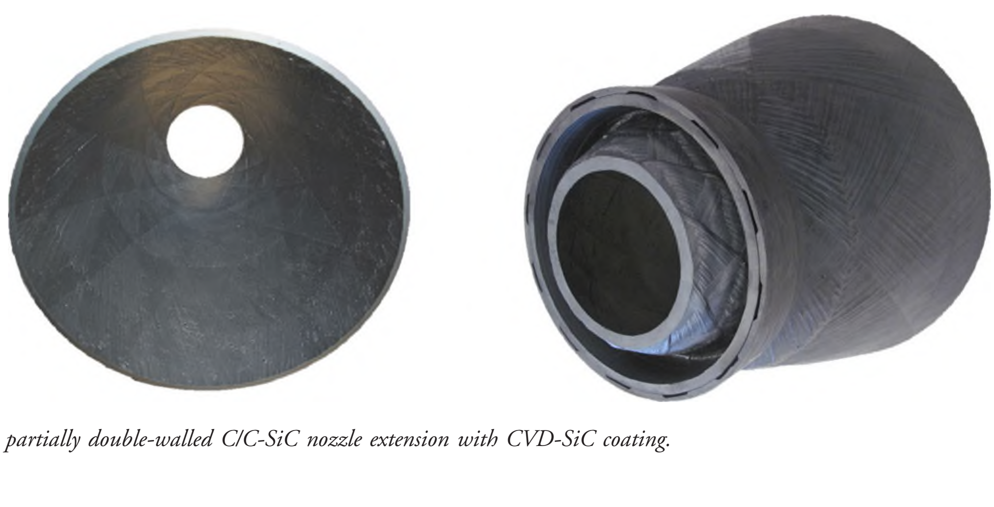

Fig. 6. Final partially double-walled C/C-SiC nozzle extension with CVD-SiC coating.

medes method. The evolution of these material properties were used to assess the manufacturing process, and will also serve as reference data which will be used for comparison during manufacture of future nozzle structures.

Computer tomography (CT)-based analysis was performed to study the pore morphology and void distribution after carbonization and siliconization, respectively. The generated CT data were also used to investigate the inner wall contour accuracy with respect to the required nozzle geometry as well as the wall thickness distribution. CT analysis was performed using VGStudioMax visualization software (Volume Graphics GmbH, Heidelberg, Germany). The final C/C-SiC microstructure was studied using an SEM; the polished specimens were cut from the nozzle exit, and interface section.

An internal pressure test with helium was carried out to demonstrate the mechanical integrity of the C/C-SiC nozzle under at least 5 bar abs. and also to determine a sufficient gas tightness with a helium leak rate lower than 1×10^{-3} mbar L/s. The C/C-SiC nozzle extension was eventually tested in preliminary hot-firing passenger tests at the test bench facility P6.2 in Lampoldshausen, Germany.

Results and Discussion

The material density and open porosity along the fabrication process are important material parameters that were determined after each processing step. Due to the wet filament winding technique, the open porosity was 10–12%, which is higher than for fabric-based CFRP processing routes, such as resin transfer molding, where CFRP specimens usually exhibit values below 5%. Within the filament winding process, issues such as parallel fiber overlapping, fiber bridging, quality of fiber impregnation, and curing without any outer molds for consolidation lead to an open porosity of the CFRP green body. During carbonization, the open porosity increased due to carbon conversion as explained in section "Manufacture". Open porosity values higher than 15% typically result in a high amount of residual silicon after the siliconization step. For this reason, the C/C preform was re-infiltrated with a second phenolic carbon precursor to reduce the amount of open porosity and consequently the amount of residual silicon. The open porosity was decreased to about 12% after the second carbonization. The final open porosity after siliconization was <3%, which resulted in a dense C/C-SiC nozzle structure with a material density of about 1.9 g/cm^3. The mass increase during siliconization was about 40%. The evolution of the material density and open porosity during the nozzle manufacture is depicted in Fig. 7.

Figure 8 presents the characteristic microstructure of the C/C-SiC nozzle material. The desired segmentation in carbon–carbon blocks was successfully realized. Note that the silicon carbide pattern (distribution and width of

Table II. Specifications of the C/C-SiC Nozzle Extension

Length	L	200 mm
Diameter	D_{Start}	68 mm
	D_{Exit}	220 mm
Expansion ratio	ε_{Start}	12
	ε_{Exit}	120
Wall thickness	t	2.5–8.0 mm
Apparent density	ρ	1.9 g/cm^3
Open porosity	e'	≈ 3%
Mass	m	≈ 900 g

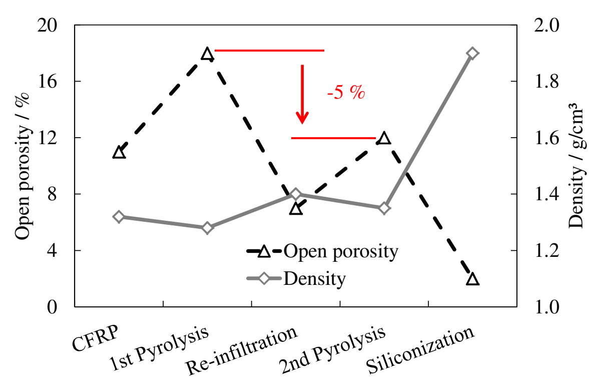

Fig. 7. Evolution of density and open porosity during the nozzle manufacture.

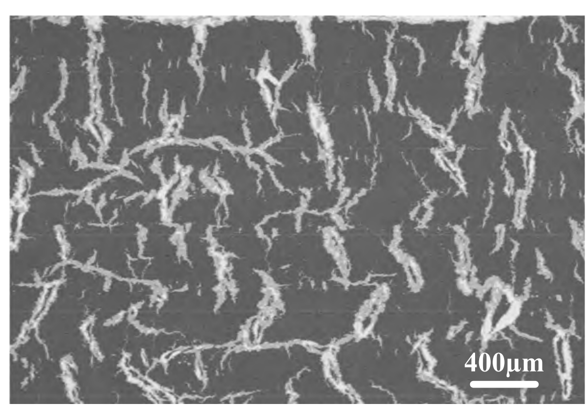

Fig. 8. Polished micrograph of the final C/C-SiC microstructure extracted from the nozzle exit (axial view direction). Phase composition (grayscale analysis): C-fiber, 55%; C, 23%; SiC, 17%; Si, 3%; and Porosity, 2%.

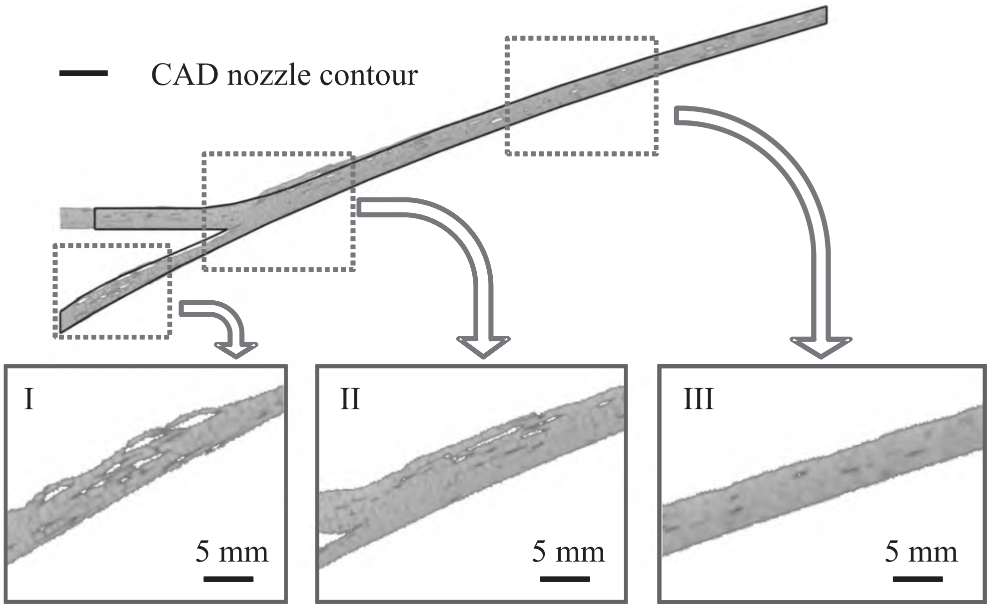

Fig. 9. Axial computer tomography images of nozzle structure after the first carbonization (C/C-skeleton).

the former inter- and intralaminar pore systems after carbonization) varied for different fiber orientations within the nozzle structure. Due to the re-infiltration of carbon after the first carbonization, the amount of residual silicon was reduced and most trans-laminar pores exhibited an increased amount of silicon carbide as a result of additional accessible carbon. The phase composition of the micrograph was determined by means of grayscale analysis using ImageJ (http://imagej.nih.gov/ij/).[2] Here, dark gray areas correspond to carbon fibers and carbon matrix. Light gray areas correspond to silicon carbide and white areas indicate residual silicon. The area fraction values are summarized in the caption of the micrograph image of Fig. 8.

Computer tomography imagery is a useful tool to investigate complex composite structures. Here, the performed CT analysis was used to evaluate any contour deformations that may occur during high-temperature processing, for flaw detection as well as for wall thickness determination.

The first CT analysis was performed after the first carbonization with a resolution (voxel size) of about 140 μm. A basic overlay of the CAD nozzle contour and the corresponding C/C nozzle structure is presented in Fig. 9; it demonstrated good agreement in the axial and radial directions, and no ovalization effects were observed. In addition, three enlarged regions of interest are shown in more detail, which illustrate some noticeable flaws. Area I is characterized by a high degree of fiber overlapping, which increases with decreasing nozzle diameters; this phenomenon created cavities. Voids detected in area II resulted from fiber bridging effects due to small winding angles in the outer fiber layers. Note, as mentioned above, that no outer molds were used for consolidation of the CFRP green body during curing, which would minimize the degree of flaws in areas with fiber bridging issues. No major imperfections were identified in areas toward the nozzle end, represented by area III which showed only minor voids that correspond to entrapped air.

Figure 10 illustrates the detected pore system after the first carbonization and in the final C/C-SiC state and visualizes the reduction of open porosity due to the liquid silicon infiltration process. Within the final C/C-SiC nozzle two areas with an increased degree of pores were detected, which were already identified as imperfections within the axial CT images (area I and II) of Fig. 9. No porosity was detected in the outer shell of the cylindrical interface area. In general, porosity was only observed in the outer layers. Figure 11 shows a circumferential CT image that demonstrates the successful manufacture of axisymmetric C/C-SiC nozzle structures without any significant delaminations or imperfections.

Figure 12 provides an overview of the procedure of superimposing CT data with the CAD target nozzle contour for a subsequent variance analysis. The consistent manufacture of a desired inner nozzle wall contour is of particular importance. Any wall contour discrepancy can

[2]ImageJ is a public domain Java image processing program.

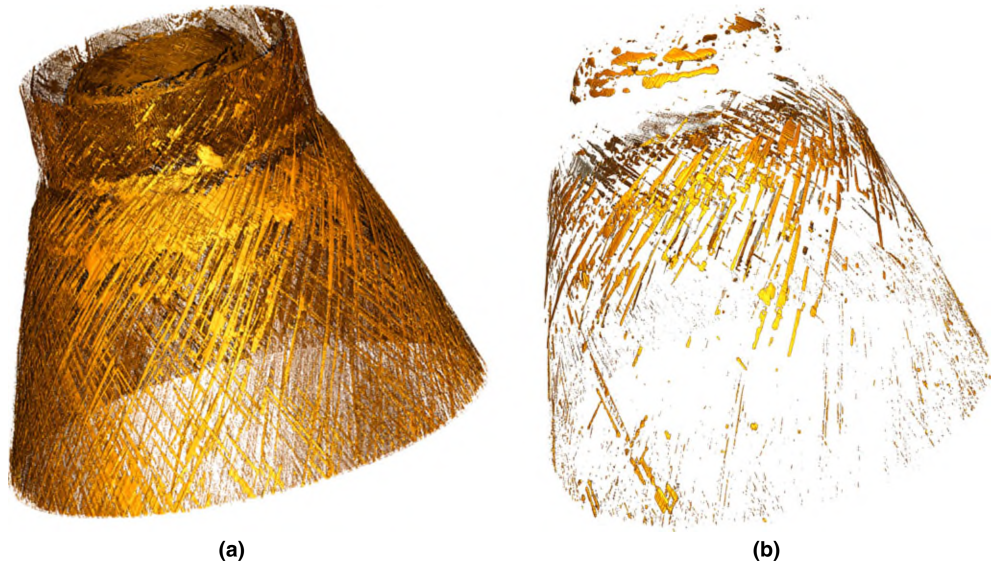

Fig. 10. Global pore morphology of the C/C body (a) and the C/C-SiC structure (b) using computer tomography (CT) imagery (CT resolution: 140 μm).

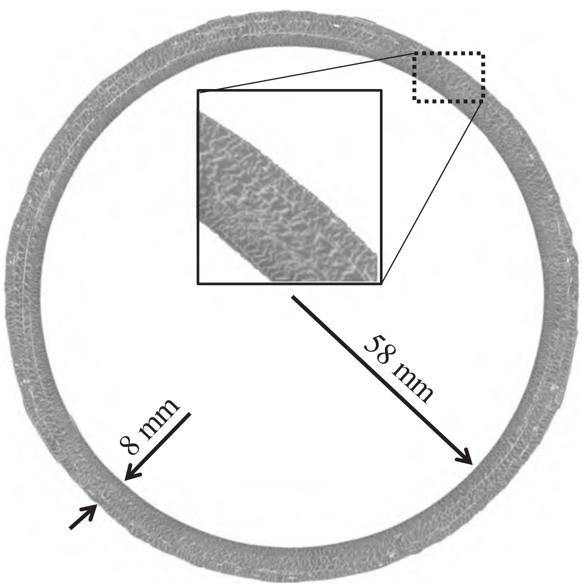

Fig. 11. Circumferential computer tomography image immediately after the connection of inner and outer shells of the final C/C-SiC nozzle structure.

be visualized with a high resolution using this superimposition technique. Figure 13 shows the result of the inner wall contour variance analysis. The manufactured contour demonstrated a very good agreement (±100 μm) for a wide surface area. Some nozzle contour deviations of more than 400 μm were identified in small nozzle diameters due to overlapping fibers. The variance analysis of the outer nozzle contour is only of minor importance.

The results of the wall thickness determination based on CT imagery are illustrated in Fig. 14. This extracted data will be used for mechanical strength estimations and FE analysis. Most parts of the nozzle showed a wall thickness in the range of 4–5 mm. The smallest wall thickness was measured in the region just before the inside shell meets the outer one. Here, the wall thickness was 2.0–2.5 mm, highlighted with red colors. With the connection of both shells, the wall thickness increased to its maximum of about 6.5–7.5 mm, marked with light blue colors. During the first carbonization the wall thickness decreased by about 10% due to the characteristic shrinkage behavior mentioned in section “Manufacture”. There were no geometry changes during siliconization.

Prior to the hot-firing tests internal pressure tests were performed to demonstrate the mechanical integrity and also to determine helium leak rates from C/C-SiC nozzle structure. Furthermore, an finite element analysis (FEA) simulation of the internal pressure test was conducted to estimate the mechanical loads. Experimental data and FEA simulation were compared.

To perform an internal pressure test of the C/C-SiC nozzle structure, an adapted breadboard was designed. The experimental setup is depicted in Fig. 15. The test required an absolute pressure of 5 bar helium. Two austenitic stainless steel plates (material: X5CrNI18-10/1.4301) were used to close the nozzle

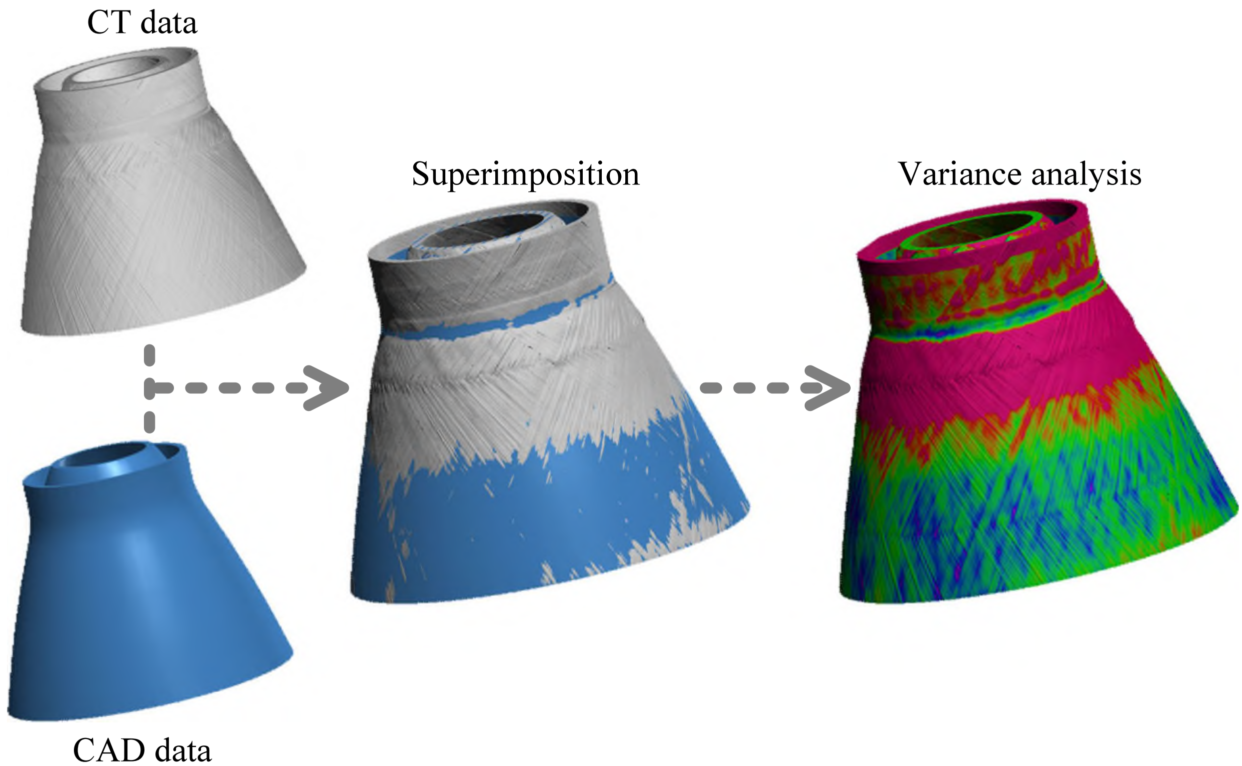

Fig. 12. Procedure of superimposing computer tomography (CT) and CAD data for variance analysis of nozzle structures.

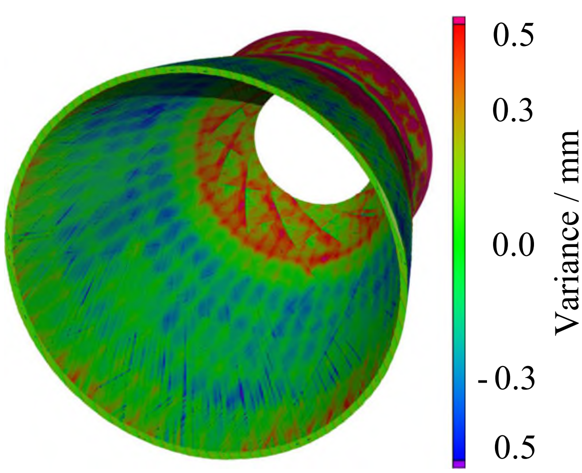

Fig. 13. High-resolution variance analysis of the manufactured inner wall contour compared to the target wall contour (best fit using visualization computer tomography software).

structure at the bottom and top. Silicone rubber pads were used to seal the interface between the bottom and the top end face of the nozzle and the steel plates. The top plate was equipped with two pressure ports. One was used as a helium feed line and the other one was used to attach a piezoresistive pressure transducer (Type 33X; Keller, Winterthur, Switzerland) for in situ pressure measurements. The leak rate was measured using a helium leak detector (Leybold UL-200; Oerlikon Leybold Vacuum GmbH, Cologne, Germany). The axial load was applied by means of a torque wrench and 12 threaded steel rods (M10). The actual axial load applied to the nozzle structure was estimated by a piezo load washer (Type 9081; Kistler, Kistler Instrumente GmbH, Ostfildern, Germany).

At four different axial positions and three different radial positions (every 120°), strain gauges were attached to the outer surface of the nozzle. The first axial position was outside of the inner shell, close to the interface (not visible in Fig. 15). Thus, in total twelve rosette strain gauges provided experimental strain measurements in axial as well as hoop directions. The test procedure was split into two load cases. The first load case only included deformations due to an applied axial force ($t = 1$). The second load case included the axial load as well as the internal pressure load ($t = 2$).

Strains were measured during the entire test procedure. Figure 16 gives an example of the experimental strain values in axial and hoop directions for the second axial position ($x = 42.9$ mm, with respect to the top) of the internal pressure test. In the first part of the test, an

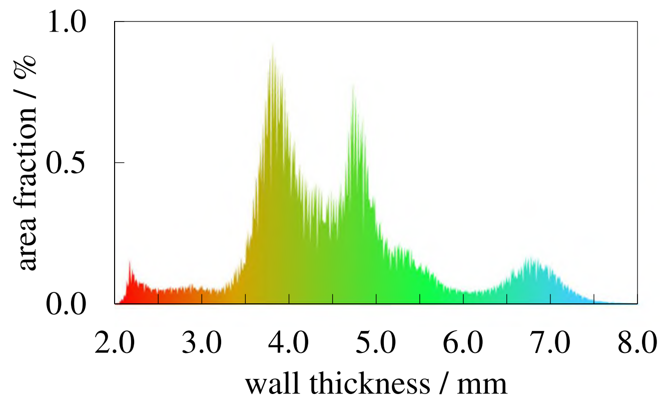

(a)

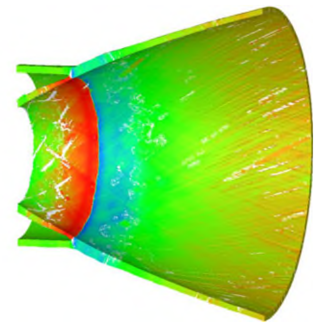

(b)

Fig. 14. Graphical (a) and structural (b) wall thickness distribution based on computer tomography imagery of the nozzle structure.

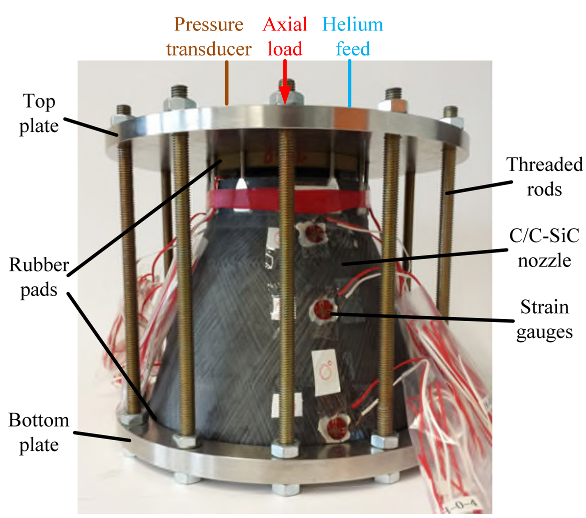

Fig. 15. Experimental setup for the internal pressure test of the C/C-SiC nozzle structure.

axial load was applied which led to an initial deformation; this represented the first load case when the required axial force was reached. This was followed by the introduction of helium gas into the nozzle, resulting in a quick increase of the internal pressure. The three strain curves of each axial position were in close range to each other, which indicated a homogeneous axial load distribution.

Average values were then calculated from the set of three strain gauges on the same axial position (mentioned above) for the first load case ($t = 1$: final axial load of approximately 7 kN) and the second load case ($t = 2$: axial load of 7 kN and an additional internal pressure of 5.3 bar abs.). The summary of the experimental strain results in which they are compared to simulated strains using FEA.

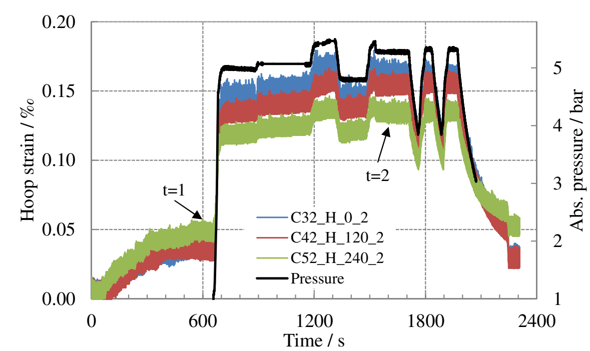

(a) Hoop strain set.

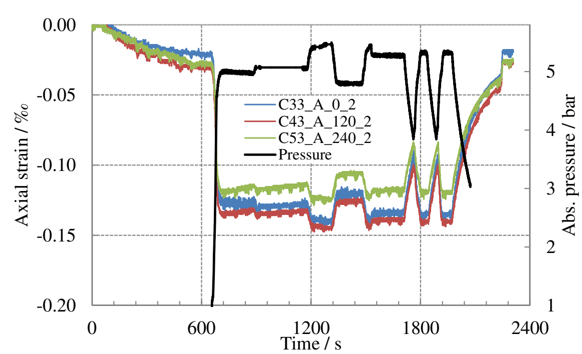

(b) Axial strain set.

Fig. 16. Example of strain measurements on the nozzle structure during the test procedure of the internal pressure test at the second axial position (x = 42.9 mm).

The helium leak rate during the performed internal pressure test was in the range of 1×10^{-3} mbar L/s, demonstrating the viability of dense C/C-SiC nozzle structures.

The main goal of analyzing the nozzle under internal pressure load in detail was to demonstrate that the structural behavior of wound C/C-SiC structures with a complex fiber architecture can be computed using finite elements. This is not self-evident, considering the complex layup produced by filament winding, the related variations in microstructure and macroscopic porosity (compare Figs. 10 and 11). As the nozzle was designed conservatively using Barlow's formula for 5 bar abs. pressure, it was not expected that failure would be indicated by FEA. Starting point for the FE model generation was a 3D-CAD file (Catia, Dassault Systèmes, Vélizy-Villacoublay Cedex, France) of the nozzle, which was generated based on the CT analysis depicted in Figs. 13 and 14. Due to the computational efficiency at complex layups, the nozzle was modeled with shell elements. Therefore, the 3D-nozzle geometry from CT analysis had to be reduced using Catia into a shell body with zero wall thickness (see nozzle shell contour sketch in Fig. 17). Each of the nine cross-wound plies was modeled as two equivalent unidirectional plies. That means instead of nine orthotropic plies, 18 unidirectional plies were modeled for the CMC nozzle structure. The local fiber orientation was imported from Cadwind software by a python script into the ANSYS Composite Preprocessing tool (ANSYS Germany GmbH, Darmstadt, Germany) (ACP). The local ply thickness was determined by dividing the true wall thickness from CT measurements (Fig. 14) by the number of UD plies at the given location. In that way the original Catia file from CT analysis was divided into 18 geometries, each representing one ply. Those CAD-geometries were then imported in ANSYS preprocessing to define the local ply thickness (Fig. 17).

The elastic input data for the UD plies was computed by inverse laminate theory[27–29] from tensile and shear tests of cross-wound ±15° C/C-SiC plates. Then, laminate theory was used to compute the elastic properties for other winding angles in order to check whether the results were persistent with further mechanical tests on cross-wound C/C-SiC plates (±30°, ±45°). The only parameter changed for data fitting was the shear modulus of ±15°. A true shear modulus for C/C-SiC with T800 fibers was not available, therefore a shear modulus for T800 composites was estimated from ±15° C/C-SiC-HTA shear modulus. Figure 18 shows a good fit

Experimental input data for a ±15° C/C-SiC (T800) composite:	
E_x (GPa)	160
E_y (GPa)	18
ν_{xy} (-)	0.7
G_{xy} (GPa)	*20**

*estimated from C/C-SiC (HTA)

ILT →

Unidirectional properties C/C-SiC (T800) derived from ILT:	
E_1 (GPa)	190.6
E_2 (GPa)	17.6
ν_{12} (-)	0.2
G_{12} (GPa)	9.8

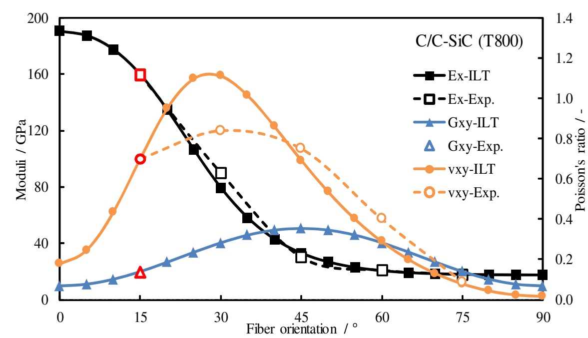

Fig. 18. Determination of UD input data by inverse laminate theory (ILT) and validation of data by classical laminate theory; the red markers represent the input data for inverse laminate theory.

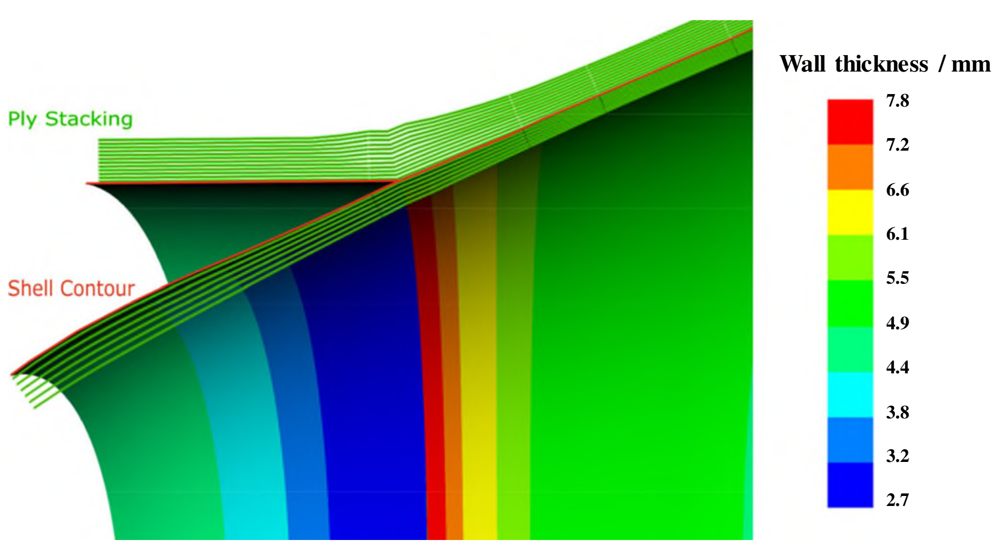

Fig. 17. Shell model generation and determination of local ply thickness.

between the experimental and computed Young's and shear moduli. There are some deviations in Poisson's ratio at ±30° fiber orientation; however, this was accepted as a good fit of moduli was prioritized over the Poisson's ratio.

Following the experimental test procedure the FEA was also divided into two load cases:

- A preload of 7 kN on a central steel rod, representing the twelve steel rods in equivalent cross section, was applied. The ANSYS functionality of screw pretension was applied on the cylindrical surface of the rod.
- Keeping the predeformation of the steel rod constant, additionally a pressure difference of 4.3 bar across the nozzle wall was defined.

All boundary conditions are visualized in Fig. 19. The interface between steel plates and C/C-SiC nozzle was modeled as frictionless contact. Figure 19 also presents the FE meshing of steel plates and C/C-SiC nozzle. Shell 181 elements (4 nodes) were used for the C/C-SiC nozzle within the commercial FEA code ANSYS 15.0. Solid 187 elements (10 nodes) were used for all steel parts.

Figure 20 summarizes the FE results in comparison with the averaged strain gauge measurements around the circumference (3 strain gauges). The stress distribution shows the hoop stress at load case 2. Overall, there is a good correlation between the strain gauge measurements and the predictions from the FE model. Particularly, good agreement was obtained in load case one. In the second load case, the FEA slightly underestimates the experimental strains, especially at the nozzle exit. This may be because of the complex boundary conditions in the experimental setup, using thick rubber pads between the steel plates and C/C-SiC nozzle structure.

Considering the complexity of the structure, the layup, and the load case, it was demonstrated that this C/C-SiC material can be modeled using an FE shell approach with virtual unidirectional C/C-SiC plies, despite variations in microstructure due to varying fiber angles.

As mentioned above, the nozzle was designed conservatively; this is proven by the FE results: The maximum strain is about 0.06%; <10% of the tensile failure strain of the equivalent cross-wound C/C-SiC plate material (±60°: 0.75%).

Relatively high strain values were reached at the intersection of inner and outer shells (risk of buckling due to low wall thickness) and at the nozzle exit caused by a stress increase with increasing diameter under internal pressure load. Those locations have to be considered if further weight reduction is aimed for.

The C/C-SiC nozzle extension was tested in preliminary hot-gas conditions for the first time within DLR's experimental full-ceramic thrust chamber test campaign at the test bench facility P6.1 in Lampoldshausen, Germany in 2013 (Fig. 21). The oxidizer/fuel ratio of the thrust chamber was expected to be 5.5 (LOX/H2) at a chamber pressure of 60 bar with a hot-gas duration of 30 s for a single test. Due to difficulties during the operation of the thrust chamber, the actual hot-gas time was drastically reduced. The accumulated hot-gas test duration of the C/C-SiC nozzle extension was about 1 min. The performed passenger tests gathered practical experience on the mounting to the thrust chamber, the integration of measurement instrumentation, and the thermomechanical performance.

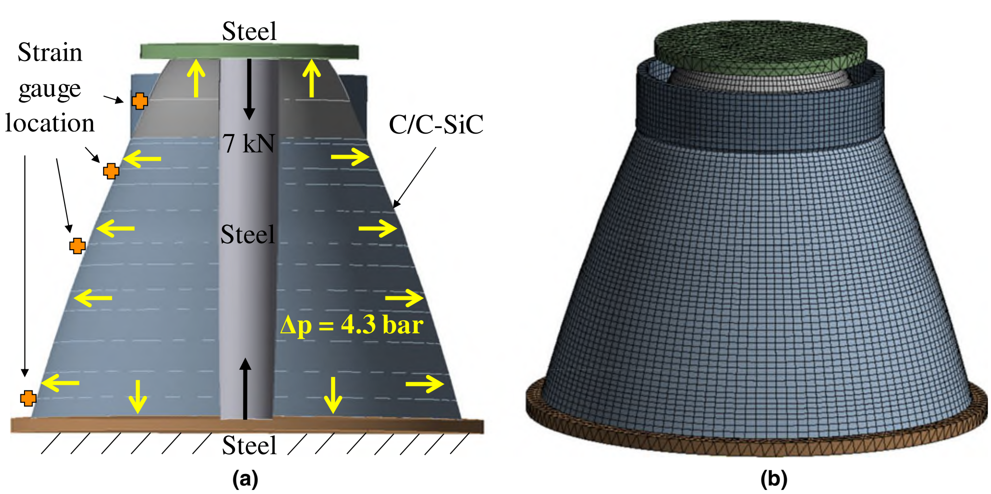

Fig. 19. Boundary conditions of two step finite element analysis; strain gauge locations from internal pressure testing are indicated (a); meshing of steel plates and C/C-SiC-nozzle (b).

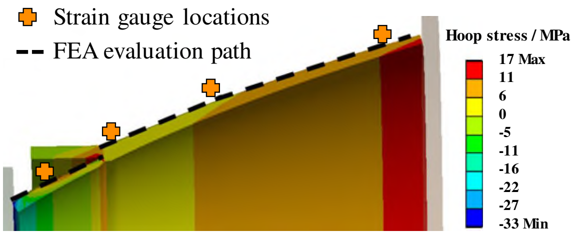

(a) FEA hoop stress distribution.

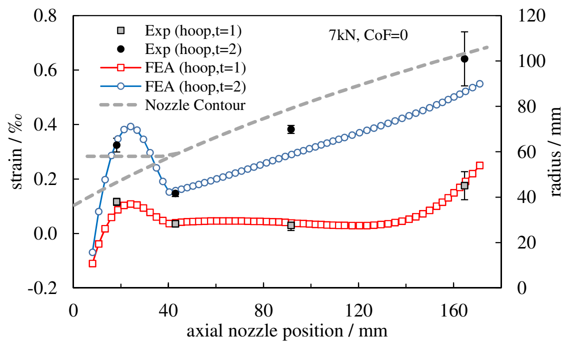

(b) Hoop strain results.

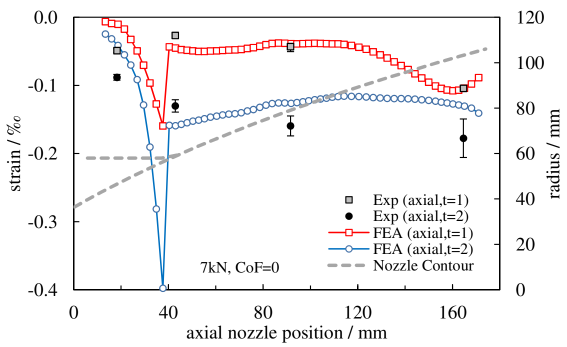

(c) Axial strain results.

Fig. 20. Stress and outer surface strain results from finite element analysis (FEA) in comparison with strain gauge measurements. The experimental strain gauge locations are indicated in the upper stress plot (load case 2). The strain results were generated from path results on the corresponding surface.

Temperature measurements were taken via nine thermocouples (Type K, NiCr–Ni) and an infrared thermometer. The thermocouples were positioned at three different radial and axial positions. The tip of the thermocouples had a distance of about 2 mm from the inner wall. Due to the transpiration-cooled nozzle throat, a certain film cooling effect was provided throughout the throat and into the nozzle extension. Therefore, relatively low maximum temperatures of about 300–450°C were observed within the C/C-SiC nozzle structure. A fully attached nozzle flow including stationary temperatures at the nozzle structure was not reached during this test

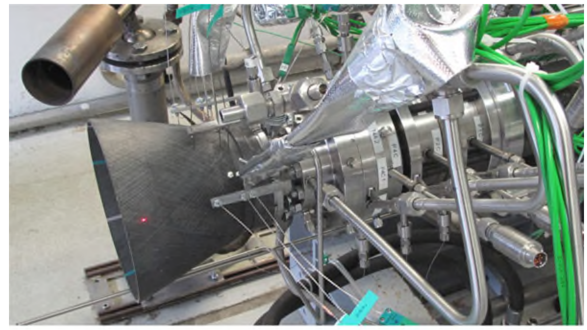

(a) Mounted to combustion chamber.

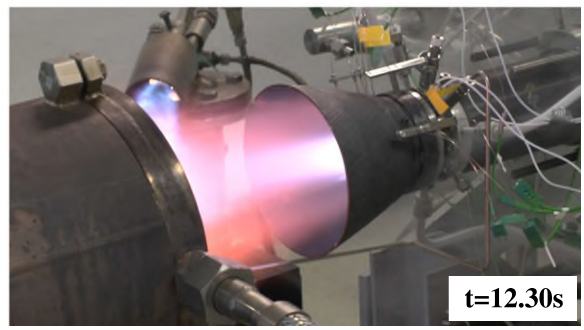

(b) During hot-firing.

Fig. 21. C/C-SiC nozzle extension at the test bench facility P6.1, DLR Lampoldshausen, Germany.

campaign. Comprehensive hot-firing and erosion tests with a successor C/C-SiC nozzle are planned for 2016.

Conclusion

For the first time, DLR demonstrated the successful fabrication of a dense, complex C/C-SiC nozzle extension using filament winding technique and an efficient adapted liquid silicon infiltration process. The inner C/C-SiC nozzle wall contour showed good agreement with the target nozzle contour, successfully demonstrating a net-shape fabrication. The manufactured C/C-SiC nozzle exhibited a density of about 1.9 g/cm^3 and an open porosity of <3% after siliconization. CT analysis identified some characteristic voids related to the filament winding technique process and curing. Improved fabrication measures, such as high shrink tapes, will reduce flaws in designated areas in future nozzle structures. Within other parts of the nozzle, no delaminations were detected. The micrograph analysis also demonstrated that the applied multi-angle fiber architecture in combination with an additional re-infiltration step leads to an improved material composition with a reduced amount of residual silicon, and low helium leak rates of about 1×10^{-3} mbar L/s. The FE analysis showed that despite microstructural variations and voids, a detailed computation of such complex C/C-SiC structures is possible. It was shown that the input data from even plates with one winding angle are consistent with the behavior of the whole structure with its multiple winding angles. The demonstrated computational approach can be used to optimize layups and further reduce component weight.

The presented manufacturing process of dense, complex CMC nozzle structures demonstrates high potential for small- and mid-size rocket nozzle applications, such as orbital engines or small upper-stage engines.

Acknowledgments

The authors gratefully acknowledge the German Research Foundation (DFG) for supporting this work within the framework of the SFB-TRR 40. The authors also appreciate the continuing support and cooperation with the Institute of Space Propulsion, DLR Lampoldshausen, Germany.

References

1. S. Beyer, S. Schmidt-Wimmer, K. Quering, M. Stein-Hilber, and C. Wilhelmi, Technology Status of Fuel Cooled Ceramic Matrix Composites for Dual-Mode Ramjet (DMR) and Liquid Rocket Engine (LRE) Applications (AIAA-2012-5877).
2. S. Beyer, S. Schmidt, F. Maidl, R. Meistring, M. Bouchez, and P. Peres, *Adv. Sci. Technol.*, 50 174–181 (2006).
3. S. Schmidt, S. Beyer, H. Immich, H. Knabe, R. Meistring, and A. Gessler, *Int. J. Appl. Ceram. Technol.*, 2 [2] 85–96 (2005).
4. J. Alting, F. Grauer, G. Hagemann, and J. Kretschmer, 37th AIAA/ASME/SAE/ASEE Joint Propulsion Conference & Exhibit (AIAA2001-3260).
5. T. Pichon, H. Coperet, A. Foucault, and A. Lacombe, 41st AIAA/ASME/SAE/ASEE Joint Propulsion Conference & Exhibit, AIAA 2005-3757, 1–11 (2005).
6. J. Wang, *et al.*, *J. Eur. Ceram. Soc.*, 29 [14] 3091–3097 (2009).
7. R. R. Naslain, *Adv. Sci. Technol.*, 50 64–74 (2006).
8. S. Tang, J. Deng, S. Wang, and W. Liu, *Mater. Sci. Eng. A Struct. Mater.*, 465 [12] 290–294 (2007).
9. J. Ma, Y. Xu, L. Zhang, L. Cheng, J. Nie, and H. Li, *Mater. Lett.*, 61 [2] 312–315 (2007).
10. E. Klatt, A. Frass, M. Frie, D. Koch, and H. Voggenreiter, *J. Eur. Ceram. Soc.*, 32 [14] 3861–3874 (2012).
11. D. M. Zhu, H. N. Du, F. Luo, and W. C. Zhou, *2006 Beijing Int. Mater. Wk*, Pts 1–4 546–549, 1501–1504 (2007).
12. K. Suresh, K. Sweety, K. Anil, S. Anupam, A. K. Gupta, and G. Rohini Devi, *Scr. Mater.*, 58 [10] 826–829 (2008).
13. J. Magnant, *et al.*, *J. Eur. Ceram. Soc.*, 32 [16] 4497–4505 (2012).
14. S. Kumar, S. Kumari, A. Kumar, A. Shukla, G. R. Devi, and A. Gupta, *Mater. Sci. Eng. A Struct. Mater.*, 528 [3] 1016–1022 (2011).
15. W. Krenkel, 25th *Annual Conference on Composites, Advanced Ceramics, Materials, and Structures: A: Ceramic Engineering and Science Proceedings*, John Wiley & Sons, Inc., Hoboken, NJ, USA, 443–454 (2008).
16. B. Heidenreich, 6th International Conference on High Temperature Ceramic Matrix Composites — HTCMC 6 (2007).
17. B. Heidenreich, Processing and Properties of Advanced Ceramics and Composites IV 183–198 (2012).
18. F. Breede, S. Hofmann, E. Klatt, and S. Denis, *Processing and Properties of Advanced Ceramics and Composites III*, Vol. 225, 3–10, JohnWiley & Sons, Inc., Hoboken, NJ, USA, 2011.
19. F. Breede, *Mechanical Properties and Performance of Engineering Ceramics and Composites VII: Ceramic Engineering and Science Proceedings*, Vol. 33, Issue 2, 183–194, John Wiley & Sons, Inc., Hoboken, NJ, USA, 2012.
20. H. Weihs, J. Longo, and J. Turner, *International Space Planes and Hypersonic Systems and Technologies Conferences*, American Institute of Aeronautics and Astronautics, Dayton, OH, 2008.
21. A. Herbertz, I. Müller, and H. Hald, *Joint Propulsion Conferences*, *American Institute of Aeronautics and Astronautics*, Atlanta, GA, USA, 2012.
22. A. Herbertz, M. Ortelt, I. Müller, and H. Hald, *CEAS Space J.*, 6 [2] 99–105 (2014).
23. S. Kumar, A. Kumar, R. B. Mala, and R. R. Mokhasunavisu, *Int. J. Appl. Ceram. Technol.*, (2015). doi: 10.1111/ijac.12392.
24. R. Wang, W. Jiao, W. Liu, F. Yang, and X. He, *Compos. Part A Appl. Sci. Manuf.*, 42 [3] 303–309 (2011).
25. S. Kumar, A. Kumar, G. R. Devi, and A. Gupta, *Mater. Sci. Eng. A Struct. Mater.*, 528 [1920] 6210–6216 (2011).
26. F. Breede, D. Koch, E. Maillet, and G. N. Morscher, *Ceram. Int.*, 41 [9, Part B] 12087–12098 (2015).
27. D. Koch, K. Tushtev, J. Horvath, R. Knoche, and G. Grathwohl, Advances in Science and Technology (Volume 45) 11th International Ceramics Congress 1435–1443 (2006).
28. O. Zebdi, R. Boukhili, and F. Trochu, *J. Reinf. Plast. Compos.*, 28 [23] 2911–2930 (2009).
29. K. Tushtev, D. Koch, and G. Grathwohl, *Int. J. Mater. Res.*, 99 [11] 1262–1267 (2008).